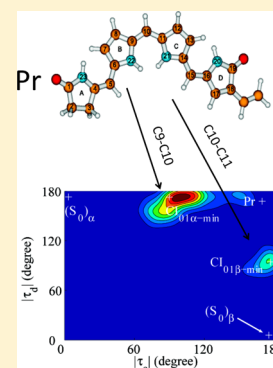


Tracking of the Molecular Motion in the Primary Event of Photoinduced Reactions of a Phytochromobilin Model

Xuhui Zhuang,^{†,‡,§} Jun Wang,^{†,‡,§} and Zhenggang Lan^{*,†,‡,§}[†]Key Laboratory of Biobased Materials, Qingdao Institute of Bioenergy and Bioprocess Technology, Chinese Academy of Sciences, Qingdao, Shandong 266101, P. R. China[‡]University of Chinese Academy of Sciences, Beijing 100049, P. R. China[§]The Qingdao Key Lab of Solar Energy Utilization and Energy Storage Technology, Qingdao Institute of Bioenergy and Bioprocess Technology, Chinese Academy of Sciences, Qingdao, Shandong 266101, P. R. China

Supporting Information

ABSTRACT: The photoinduced processes of phytochromes have received great research interest for their important biological functions. Phytochromobilin (PΦB), one of the most important phytochrome chromophores, was selected as the prototype to study its photoinduced isomerization. The nonadiabatic dynamics of PΦB from the Pr configuration in the gas phase was investigated by the surface hopping method at the OM2/MRCI level. In the excited state, isolated PΦB does not display the rotation of the two terminal five-membered rings (ring A and ring D), which is assumed to govern the Pr → Pfr process in the protein. Instead, two S_1/S_0 conical intersection seams ($CI_{01\alpha}$ and $CI_{01\beta}$) characterized by the rotation of the two central rings (ring B and ring C) were proven to play essential roles for the photoisomerization of PΦB in the gas phase. These two conical intersections ($CI_{01\alpha}$ and $CI_{01\beta}$) are accessible by the twisting motions of the C9–C10 and C10–C11 bonds, respectively. The $CI_{01\alpha}$ and $CI_{01\beta}$ seams, instead of their minimum-energy points, are responsible for the nonadiabatic dynamics. For both channels, the trajectories may propagate forward to the isomerization products or backward to the original Pr configuration after the $S_1 \rightarrow S_0$ hops.



1. INTRODUCTION

Phytochromes represent a widely existing group of important photoreceptors in plants, bacteria, and fungi. These photoreceptors can serve as bioclocks to regulate the fundamental functions of plants and other autotrophs, such as seed germination, growth, phototaxis, pigmentation, and so on.¹ Thus, some important phytochromes have been investigated frequently in the last decades.^{1–4} From these studies, it is well-known that the functionality of phytochromes is governed by switching between two photoconvertible forms, namely, the physiologically inactive red form (Pr) and the physiologically active far-red form (Pfr), which show maximum photo-absorptions in the red (~660 nm) and far-red (~730 nm) regions, respectively.¹ The photoreaction centers of phytochromes were also identified and are composed of an open-chain tetrapyrrole chromophore, such as phytochromobilin (PΦB), phycocyanobilin (PCB), or biliverdin (BV), surrounded by protein residues (Figure 1).

Besides photoreceptors, the open-chain tetrapyrrole chromophores also play essential roles in light-harvesting systems and energy-transfer intermediates in antenna complexes.⁴ Moreover, these chromophores are analogues of porphyrins, which represent another type of photoactive compounds with biological importance. The porphyrins and the phytochrome chromophores can be biosynthetically converted via ring opening reactions or vice versa.⁴

The phytochrome chromophores have many isomers because of the existence of many twistable single and double C–C bonds in such open-chain tetrapyrrole systems. This makes identifying their configurations a very challenging problem. As discussed in previous studies,¹ the Z/E isomerization happens at the double bonds of C4–C5, C10–C11, and C15–C16, while the symmetry/antisymmetry (s/a) isomerization exists at single bonds such as C5–C6, C9–C10, and C14–C15. By using this rule, we can easily define the conformation of any isomer. In last decades, many pioneering works were devoted to determining the molecular configurations of the Pr conformation of different phytochrome chromophores.¹ Among them, the Pr conformations of BV (in bacteria) and PCB (in cyanobacteria) were identified as the ZsZsZa stereoisomer (C5–Z,syn C10–Z,syn C15–Z,anti; see Figure 1) by crystallography and NMR spectroscopy,^{5–10} while the Pr conformation of PΦB (in plant) was assigned as the ZaZsZa stereoisomer (C5–Z,anti C10–Z,syn C15–Z,anti; see Figure 2) by resonance Raman (RR) spectroscopy.^{11,12}

In contrast to the well-known configuration of the Pr form, the structure of the Pfr conformation seems to be controversial and is assumed to depend on the reaction mechanisms of the photoinduced Pr → Pfr conversion processes in different

Received: September 2, 2013

Revised: November 20, 2013

Published: November 21, 2013

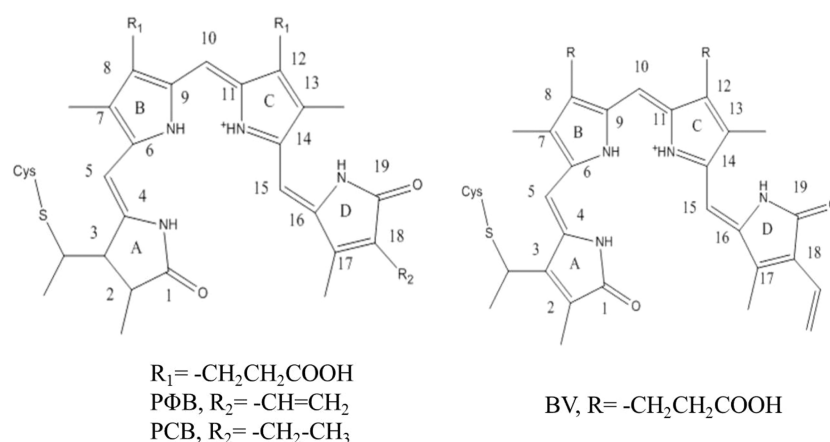


Figure 1. Chemical structures of biliverdin (BV), phycocyanobilin (PCB), and phytochromobilin (PΦB) in the ZsZsZa configuration.

biological systems. Therefore, the study of photoinduced Pr \rightarrow Pfr reactions becomes a very important topic not only for the understanding of the photoisomerization processes but also for the assignment of the resulting Pfr structures.

The Pr \rightarrow Pfr conversions of phytochrome chromophores in protein environments have been widely investigated experimentally. Although the mechanism of photoinduced Pr \rightarrow Pfr isomerization of phytochromes is still controversial,¹³ many studies have agreed that the photoisomerization includes two reaction steps. In step 1, the Z \rightarrow E photoisomerization at the C15–C16 double bond plays the key role, and this step gives the so-called “Lumi-R” intermediate.^{11,14–19} In step 2, the “Lumi-R” intermediate can convert to the Pfr isomer via thermal reactions (internal rotation around the C14–C15 bond).^{15,16,18,19} But some researchers believed that the second step (the thermal one) may involve the twisting motion of the C5–C6 bond between ring A and ring B.^{11,12} Since it is still very difficult to get more detailed information, some scientists have tried to investigate the configurations of the Pr form and the Pr \rightarrow Pfr conversion mechanisms by theoretical calculations. These efforts include the investigation of the stability of different conformations by electronic structure calculations, the examination of the role of protein environments by molecular dynamics, and the simulation of spectroscopies at different levels of theory.^{11,12,19–24} These studies agreed that the Pr \rightarrow Pfr interconversion in protein environments is triggered by the Z \rightarrow E photoisomerization at the C15–C16 bond.

In recent years, great efforts have been devoted to clarifying the photoinduced isomerization mechanism in phytochromes at the atomic level from chemical aspects. However, such efforts are very challenging because the phytochromes contain very complex proteins. Thus, some efforts were devoted to studying the chromophores themselves, since they are responsible for the primary events in the photoinduced biological cycle of phytochromes.^{2,14,15,19,23,25–30} In addition, the phytochrome chromophores consist of only four open-chain tetrapyrroles, and the nonconjugated side groups should have only minor influences on the initial photoabsorption and successive isomerizations. Thus, some chemists, especially theoretical scientists, have attempted to choose isolated chromophores as typical models to investigate the photoisomerization mechanisms of phytochromes. As the most important photoreceptor in plants, PΦB has often been chosen as such a prototype system,^{2,14,15,19,23,25–30} and its photoisomerization mechanism

has also been studied without considering the protein moiety.^{2,28,30} Interestingly, these studies found that the photoconversion mechanism seems to be completely different with or without the presence of the original protein environments. Instead of the double-bond twist at the C15–C16 bond, the rotation of ring B and ring C seems to be rather easier to access in vacuo. Such a difference may be caused by the steric hindrance of protein environments. As suggested by previous work,³⁰ ring A and ring B are fixed by the protein-binding pocket, while ring D becomes the “free moiety” that can perform the rotation. In vacuo, however, the steric hindrance is wiped off, and all four of the five-membered rings are free. Furthermore, the electrostatic repulsion between rings B and C reinforces their separation.³⁰ Therefore, the rotation of ring B or ring C takes place for PΦB.

Despite the large number of studies, the primary events in the initial step of the photocycle of phytochromes are still not fully understood. Because of the complexity of such systems, it is difficult to examine all of the details from currently available experimental and theoretical data. Furthermore, the precursors proved only that the rotation between ring B and ring C is a key factor for PΦB in the gas phase; they did not determine which central bond (C9–C10 or C10–C11) experiences the twisting motion.¹ Some works suggested that the internal rotation around the C10–C11 bond dominates the photoinduced conversion, but their studies did not take the twist of the C9–C10 bond into account.^{28,30} Thus, the elucidation of these isomerization processes certainly requires the direct examination of the excited-state dynamics of PΦB.

As our first step to investigate the photoinduced reactions of phytochromes, we performed nonadiabatic dynamics simulations of a PΦB model in vacuo using the on-the-fly surface hopping method^{31–33} at the semiempirical OM2/MRCI level.^{34–37} Since a large number of electronic-structure calculations at a reliable level are required for on-the-fly trajectory calculations, it is important to apply a quantum-chemistry method that can provide a reasonable compromise between computational cost and accuracy. For this purpose, the OM2/MRCI method was chosen since many benchmark calculations have shown that it can provide a reasonable description of molecular excited states with rather low computational cost.^{34–36} Although it was reported that the OM2/MRCI method may not always be very accurate for some systems,³⁸ the nonadiabatic dynamics simulation at the OM2/MRCI level should still be a powerful and meaningful tool for

many cases after careful benchmark calculations.^{39–43} Thus, some necessary high-level electronic calculations were also performed for benchmark reasons.

In this work, we studied the photoinduced isomerization of a PΦB model. For simplicity, only the excited-state dynamics starting from the Pr conformation was considered. By tracking the real-time nuclear motion, we tried to provide a detailed understanding of the photoisomerization of the phytochrome chromophores in vacuo. This work can become an important reference for understanding the photoinduced reactions of phytochrome chromophores within biological environments and to determine the roles of the protein residues in the Pr → Pfr photoconversion. In addition, the current work should also provide useful information on the other tetrapyrrole analogue systems such as porphyrin and its derivatives.

2. COMPUTATIONAL DETAILS

2.1. Molecular Model Construction. Several configurations exist for PΦB because of the presence of many single and double C–C bonds. The RR studies of plant phytochromes have proven that the Pr form of PΦB takes the ZaZsZa conformation.^{11,12} Thus, the current work also employed the ZaZsZa configuration for Pr. To reduce the computational cost, we used the simplified PΦB model reported in refs 28 and 30 (Figure 2): some side groups (the C3 thioether linkage, the C8

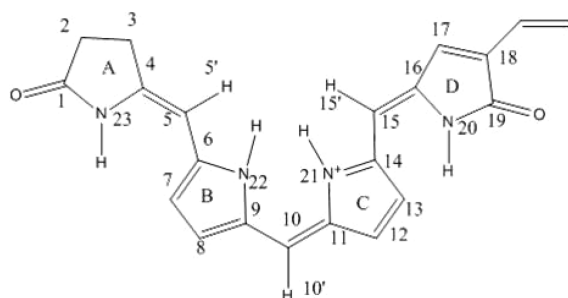


Figure 2. PΦB model in Pr (ZsZsZa) configuration.

and C12 propionic carboxyl groups, and the C2, C7, C13, and C17 methyl groups) were replaced by hydrogen atoms for simplicity. In principle, these side groups should not be conjugated with the four five-membered rings and should hardly influence the conjugation of PΦB. The N atom in ring C is also protonated as in the earlier reports.^{28,30} In order to illustrate the photoisomerization procedure conveniently, we defined several key internal coordinates, such as the important bond lengths and dihedral angles, as shown in Table 1. The symbols d_{4-5} , d_{5-6} , d_{9-10} , d_{10-11} , d_{14-15} , and d_{15-16} denote the bond lengths of C4–C5, C5–C6, C9–C10, C10–C11, C14–C15, and C15–C16, respectively. The variables τ_{4-5} , τ_{5-6} , τ_{9-10} , τ_{10-11} , τ_{14-15} and τ_{15-16} denote the twisting angles around C4–C5, C5–C6, C9–C10, C10–C11, C14–C15, and C15–C16, respectively.

2.2. Electronic-Structure Calculations. The semiempirical calculations were performed using the MNDO99 program.⁴⁴ The Gaussian 09⁴⁵ and TURBOMOLE 6.5⁴⁶ programs were also used in the benchmark calculations.

2.2.1. Semiempirical Method. The orthogonalization model 2 (OM2) method was applied to build the semiempirical electronic Hamiltonian.^{34–36} The multireference configuration interaction (MRCI) method was used to describe the excited-state wave functions.³⁷ The self-consistent field (SCF)

Table 1. Definitions of the Key Geometric Parameters

definition	internal coordinate	relative mode
d_{4-5}	C4–C5 distance	C4–C5 bond length
d_{5-6}	C5–C6 distance	C5–C6 bond length
d_{9-10}	C9–C10 distance	C9–C10 bond length
d_{10-11}	C10–C11 distance	C10–C11 bond length
d_{14-15}	C14–C15 distance	C14–C15 bond length
d_{15-16}	C15–C16 distance	C15–C16 bond length
τ_{4-5}	N23–C4–C5–H5' dihedral angle	twist of C4–C5
τ_{5-6}	N22–C6–C5–H5' dihedral angle	twist of C5–C6
τ_{9-10}	N22–C9–C10–H10' dihedral angle	twist of C9–C10
τ_{10-11}	N21–C11–C10–H10' dihedral angle	twist of C10–C11
τ_{14-15}	dihedral angle N21–C14–C15–H15'	twist of C14–C15
τ_{15-16}	N20–C16–C15–H15' dihedral angle	twist of C15–C16

calculations were performed in the basis of the restricted open-shell Hartree-Fock (ROHF) formalism, since it provides the better treatment of molecular excited states. At the OM2/MRCI level, the potential energies (PEs) of relevant electronic states and their gradients and nonadiabatic couplings were calculated analytically. Three references (the closed shell and the single and double HOMO–LUMO excitations) were used to build all of the configurations in the MRCI expansion, and all of the single and double excitations from these three references were included in the configuration-interaction treatment. The active space (AS) in the MRCI included 16 electrons in 12 orbitals [(16,12)]: six π orbitals, two n orbitals and four π^* orbitals.

Geometry optimizations of the ground-state and the excited-state minima were performed using the Newton–Raphson iteration scheme. The minimum-energy structures of conical intersections (CI) were obtained using the Lagrange–Newton method.^{47–49}

The minimum-energy CI geometry (obtained from CI optimization) was taken as the starting point, and the two-dimensional (2D) rigid scans of PE surfaces were performed along two relevant dihedral angles. Then the crossing of two PE surfaces gave us the CI seam within the two-dimensional space spanned by two dihedral angles. This seam might not be the minimum-energy CI seam within this two-dimensional space, while the former should be a good approximation of the latter. In the discussion below, we used the former choice since it provides more information on the topology of the two PE surfaces. As a complementary investigation, we also constructed the minimum-energy CI seams using constrained CI optimization by fixing the major reaction coordinates τ_{9-10} and τ_{10-11} , respectively (Figure S-4 in the Supporting Information).

2.2.2. High-Level Calculations. In benchmark steps, single-point calculations at critical points were performed at the ADC(2)/TZVP level^{50,51} based on the OM2/MRCI geometries. We also attempted to use the DFT/TDDFT method (B3LYP^{52,53}/6-31+G*) to optimize critical points and calculate excitation energies.

2.3. Nonadiabatic Dynamics. The photoinduced non-adiabatic decay dynamics was studied by trajectory surface-hopping simulations at the OM2/MRCI level. The non-adiabatic transition was treated using Tully's fewest-switches algorithm.³¹ A set of initial conditions (geometries and velocities) was generated from the Wigner distribution function of normal modes. The initial conditions were then created by putting these snapshots into the S_1 state vertically. All of the

Table 2. Internal Coordinates [Bond Distances (Å) and Dihedral Angles (deg)] at Critical Structures^a

geometry	d_{9-10}	d_{10-11}	τ_{5-6}	τ_{9-10}	τ_{10-11}	τ_{14-15}	τ_{15-16}
Pr	1.39	1.40	−17.9	−167.9	−167.2	−17.5	173.9
(S ₀) _α	1.40	1.40	−19.5	1.1	−179.5	17.7	−174.1
(S ₀) _β	1.39	1.40	21.3	−177.8	4.0	−19.9	174.1
(S ₁) _α	1.45	1.38	−8.5	−90.9	−177.6	14.0	−173.5
(S ₁) _β	1.38	1.45	−18.1	−176.7	−92.0	−7.4	170.4
CI _{01α-min}	1.45	1.38	−7.8	−91.5	−177.2	−13.1	173.7
CI _{01β-min}	1.38	1.45	−21.1	−176.1	−93.1	−6.0	−167.1

^aThe structure of (S₀)_α was optimized from the geometry obtained by twisting the C9–C10 bond about 180° from the Pr conformation; (S₀)_β was obtained by performing the same procedure on the C10–C11 bond.

Table 3. S₀ and S₁ Energies (eV), S₀ → S₁ Vertical Excitation Energies (eV), and Oscillator Strengths (in Parentheses) for Critical Geometries at the OM2/MRCI, B3LYP/6-31+G*, and ADC(2)/TZVP Levels

geometry	OM2/MRCI			B3LYP/6-31+G*			ADC(2)/TZVP		
	S ₀	S ₁	S ₀ → S ₁	S ₀	S ₁	S ₀ → S ₁	S ₀	S ₁	S ₀ → S ₁
Pr	0.10	2.38	2.28 (1.04)	0.07	2.21	2.14 (1.70)	0.03	1.98	1.95 (1.56)
(S ₀) _α	0.00	2.30	2.30 (1.07)	0.01	2.14	2.13 (1.98)	0.01	1.96	1.95 (1.84)
(S ₀) _β	0.08	2.44	2.36 (1.10)	0.00	2.13	2.13 (1.91)	0.00	1.97	1.97 (1.83)
(S ₁) _α	1.43	1.56	0.13 (0.00)				1.43	1.82	0.39 (0.00)
(S ₁) _β	1.31	1.55	0.24 (0.00)				1.28	1.86	0.58 (0.00)
CI _{01α-min}	1.58								
CI _{01β-min}	1.56								

relevant energies, gradients, and nonadiabatic couplings were calculated analytically in the manner of “on-the-fly”. The step times were 0.1 fs for the nuclear motion and 0.001 fs for the electronic propagation. The final results were obtained by averaging over all 127 trajectories.

3. RESULTS AND DISCUSSION

3.1. Properties of the Pr Conformation. The geometry of the PΦB model in the Pr configuration (ZaZsZa) was optimized at the OM2/MRCI level, as shown in Figure S-1 in the Supporting Information and Table 2. As expected, both C4–C5 and C15–C16 have double-bond character (~1.37 Å), while C5–C6 and C14–C15 retain single-bond character (~1.43 Å). In contrast, the two central bonds (C9–C10 and C10–C11) display similar bond lengths (1.39 and 1.40 Å), reflecting the equal share of the positive charge by rings B and C rather than rings A and D. These geometrical features are consistent with the data obtained at the B3LYP level and previous reports.^{2,28,30} The S₀ → S₁ vertical energy in the Pr configuration is 2.28 eV (Table 3), which is also consistent with reference results^{28,30} and our own benchmark data at the B3LYP/6-31+G* (2.14 eV) and the ADC(2)/TZVP (1.98 eV) levels.

Previous references reported that one S₁ minimum named “PLA” exists in the Franck–Condon region and that its geometry is close to the Pr conformation (ZaZsZa). In previous work, such a minimum was obtained successfully at the TDDFT (TD-B3LYP/SVP, numerical gradient), CIS, and CASSPT2 levels.^{2,28} Unfortunately, the PLA (S₁)_{min} could not be found at the OM2/MRCI level, and the optimization starting from the Pr configuration finally crashed at the geometry close to the S₁/S₀ CI characterized by the rotation around C10–C11 up to ~90°. To check the discrepancy, we attempted to optimize the PLA at the TDDFT level under different conditions, such as using different density functionals, several types of basis sets, the random phase approximation (RPA) and the Tamm–Dancoff approximation (TDA), and a

numerical or analytical gradient (Table S-3 in the Supporting Information). It turned out that the existence of the PLA was highly dependent on above factors. In some cases, we could optimize the PLA successfully. For example, the PLA could be optimized at the PBE0/def2-SVP level using a numerical or analytical gradient within the RPA and TDA. However, in some other cases (e.g., at the PBE0/TZVP level using a numerical or analytical gradient within the RPA and TDA), the optimization drove the system to leave the Franck–Condon region and perform the C10–C11 twist until the job finally crashed at the geometry with a very small S₁/S₀ energy gap. This implies that the S₁ PE surface in the Franck–Condon region is very flat. In this case, even if the PLA exists, this S₁ minimum should be very shallow and not stable. Previous work also found the similar feature in their reaction-path scans.² Since the PE surface is rather flat in the Franck–Condon region, the excited-state dynamics should not be highly influenced by whether a very shallow S₁ minimum exists or not. In view of the reasonable geometries and energies (see section 3.2 below), we believe that the OM2/MRCI method still can provide a reliable description of the molecular motion in the nonadiabatic dynamics of the PΦB model.

3.2. Potential Energy Surface. Our preliminary non-adiabatic dynamics study found two photoreaction channels: the internal rotation around C9–C10 and the internal rotation around C10–C11 (see section 3.3). Since the twisting motion of the C15–C16 bond dominates the photochemical reaction of Pr in proteins, it was also considered. The three one-dimensional PE surfaces along the three isomerization paths (C9–C10, C10–C11, and C14–C15) were constructed (Figure S-2 in the Supporting Information). The former two pathways, involving the C9–C10 and C10–C11 twists (Figure S-2a,b) are barrierless from the Pr conformation to the corresponding CIs, while the third one (Figure S-2c) is unfavored. Previous theoretical studies on the excited-state reaction pathway of the PΦB model in the gas phase also suggested a similar mechanism.^{2,28,30} Thus, in this section our

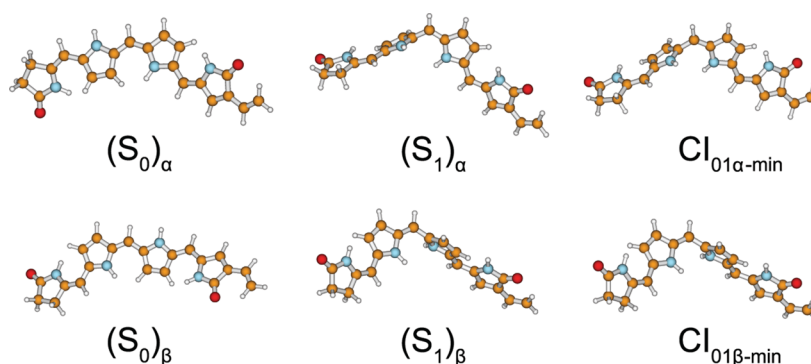


Figure 3. Optimized geometries of two ground-state minima [$(S_0)_\alpha$ and $(S_0)_\beta$], two lowest singlet excited-state minima [$(S_1)_\alpha$ and $(S_1)_\beta$], and two S_1/S_0 conical intersection minima [$CI_{01\alpha\text{-min}}$ and $CI_{01\beta\text{-min}}$] at the OM2/MRCI level of theory.

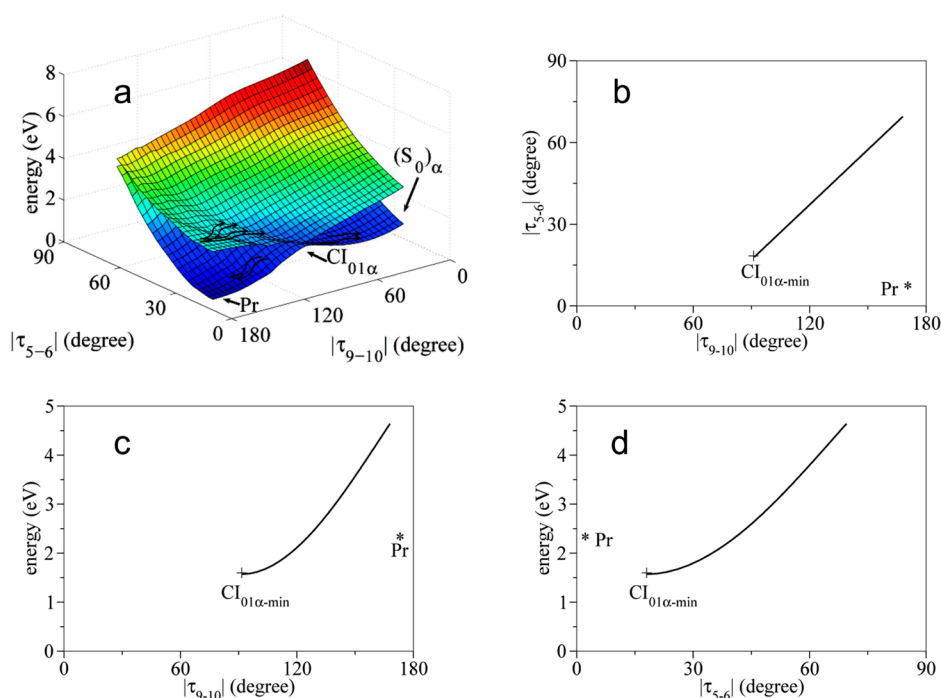


Figure 4. Reaction paths from the Pr conformation to $(S_0)_\alpha$. (a) Two-dimensional PE surfaces as functions of τ_{9-10} and τ_{5-6} . (b) Profile of the $CI_{01\alpha}$ seam in the space spanned by τ_{9-10} and τ_{5-6} . (c, d) PE surfaces of the $CI_{01\alpha}$ seam as functions of τ_{9-10} and τ_{5-6} , respectively. τ_{5-6} and τ_{9-10} in the plot denote the dihedral angles around C5–C6 and C9–C10, respectively. “+” in the plot refers to the location of $CI_{01\alpha\text{-min}}$, and “*” in the plot shows the vertical excitation energy of Pr.

work focused only on the PE surfaces along reactive coordinates responsible for two observed major channels (internal rotations around C9–C10 and C10–C11) and did not address others.

3.2.1. Channel I. One S_0 minimum with the ZsZsZa conformation, $(S_0)_\alpha$ is located at the OM2/MRCI level when the whole A–B double-ring moiety rotates around the C9–C10 bond by about 170° (Figure 3 and Table 2). The energy of $(S_0)_\alpha$ is 0.10 eV lower than that of the Pr conformation at the OM2/MRCI level, and the $S_0 \rightarrow S_1$ vertical excitation energy is 2.30 eV at $(S_0)_\alpha$. Since similar data were also obtained at the ADC(2)/TZVP and B3LYP/6-31+G* levels (Table 3), the OM2/MRCI result is reliable.

At the OM2/MRCI level, one S_0/S_1 CI minimum ($CI_{01\alpha\text{-min}}$, 1.68 eV above Pr) is located by the rotation of the A–B double-ring moiety around the C9–C10 bond by about 80° from the Pr conformation (Figure 3 and Tables 2 and 3). From the Pr to $CI_{01\alpha\text{-min}}$, the other central C–C bond (C10–C11) performs

only a weak twisting (τ_{10-11} from -167.2° to -177.2°). During this rotation, the angle between rings A and B becomes smaller (τ_{5-6} from -17.9° to -7.8°). This indicates that both the twisting motion of the central C10–C11 bond and the reduction of the ring A/ring B angles are required to access $CI_{01\alpha\text{-min}}$. The C9–C10 bond distance increases from 1.39 to 1.45 Å, while the C10–C11 bond distance becomes shorter from 1.40 to 1.38 Å. Therefore, C9–C10 and C10–C11 tend to become single and double bonds, respectively. At this geometry, the intramolecular charge transfer is indicated by the molecular orbitals (Figure S-3 in the Supporting Information) and net atomic charge distributions (Table S-5 in the Supporting Information), also consistent with the reference reports.^{28,30}

One S_1 minimum, $(S_1)_\alpha$ is present in the vicinity of $CI_{01\alpha\text{-min}}$. The major geometry distinction between $(S_1)_\alpha$ and $CI_{01\alpha\text{-min}}$ is that they show different angles between rings C and D. From Pr to $(S_1)_\alpha$ the twisting angle of the C14–C15 bond (τ_{9-10})

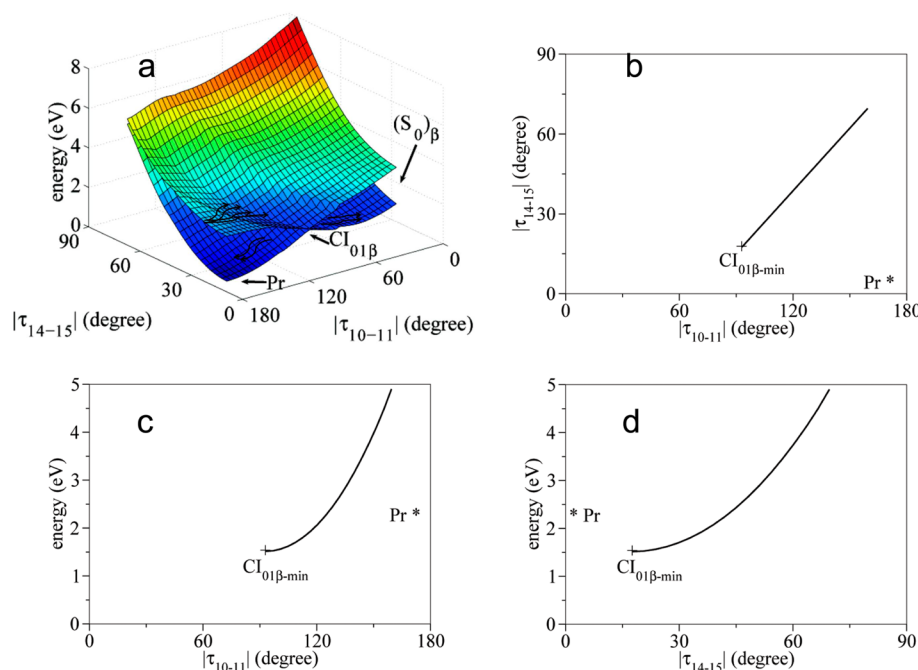


Figure 5. Reaction paths from the Pr conformation to $(S_0)_\beta$. (a) Two-dimensional PE surfaces as functions of τ_{10-11} and τ_{14-15} . (b) Profile of the $CI_{01\beta}$ seam in the space spanned by τ_{10-11} and τ_{14-15} . (c, d) PE surfaces of the $CI_{01\beta}$ seam as functions of τ_{10-11} and τ_{14-15} , respectively. τ_{10-11} and τ_{14-15} in the plot denote the dihedral angles around C10–C11 and C14–C15, respectively. “+” in the plot refers to the location of $CI_{01\beta-min}$, and “*” in the plot shows the vertical excitation energy of Pr.

changes from -17.5° to 14.0° , which is much bigger than the change from Pr to $CI_{01\alpha-min}$ (τ_{9-10} from -17.5° to -13.1°). At the $(S_1)_\alpha$ geometry, the S_0 – S_1 energy gap is very small (only ~ 0.13 eV), which indicates that $(S_1)_\alpha$ is close to the S_0/S_1 CI. Since DFT failed at the configuration with a small S_0 – S_1 energy gap, all attempts to optimize $(S_1)_\alpha$ at the TDDFT level crashed no matter which functional was selected. We performed only single-point ADC(2) calculations at the $(S_1)_\alpha$ geometry in the benchmark step. At the ADC(2) level of theory, the S_0 – S_1 energy gap was also found to become very small (Table 3).

It is well-known that nonadiabatic transitions do not necessarily take place at the minimum-energy geometry of a CI. Instead, all accessible regions of the CI seam should be responsible. Thus, we attempted to check the topology of the CI seam. The 2D PE surfaces were constructed by performing rigid scans along internal coordinates τ_{9-10} and τ_{5-6} starting from the Pr form (Figure 4).

Starting from the Pr conformation, it is easy to access $CI_{01\alpha}$ in the S_1 state because this channel is almost barrierless (Figure 4a). It should be possible to derive the reaction mechanism of channel I from the PE surface profiles and the CI topology. After the molecule is excited to the S_1 state at the Pr conformation, it relaxes to the $CI_{01\alpha}$ seam by rotation of ring B around the C9–C10 bond (τ_{9-10}) and ring A around the C5–C6 bond (τ_{5-6}). After its decay to the S_0 state at the $CI_{01\alpha}$ seam, the molecule may experience further rotation of ring B forward to $(S_0)_\alpha$ or backward to Pr ultimately. Interestingly, the $CI_{01\alpha}$ seam exhibits a line in the two-dimensional space spanned by τ_{9-10} and τ_{5-6} (Figure 4b). It is also interesting to notice that the vertical excitation energy of Pr is above a part of the CI seam (range from 2.28 to 1.58 eV in Figure 4c,d). Thus, the excited-state PE surface may drive the system toward not only $CI_{01\alpha-min}$ but also the $CI_{01\alpha}$ seam. In other words, the angle between rings B and A may also play an essential role in the

excited-state dynamics in addition to the twisting motion of the C9–C10 bond.

3.2.2. Channel II. At the OM2/MRCI level, one S_0 minimum displaying the ZaEsZs conformation, $(S_0)_\beta$, is also obtained by rotation of the whole C–D double-ring moiety by about 170° around the C10–C11 bond (Figure 3 and Table 2). All three S_0 minima in the current work [Pr, $(S_0)_\alpha$, and $(S_0)_\beta$] are located in a similar energy range at the OM2/MRCI, B3LYP/6-31+G*, and ADC(2)/TZVP levels. For $(S_0)_\beta$, the vertical excitation energy of S_1 is 2.36 eV at the OM2/MRCI level, consistent with the B3LYP/6-31+G* (2.13 eV) and ADC(2)/TZVP (1.97 eV) results. Similar to channel I, the consistent data obtained at the OM2/MRCI, DFT/TDDFT, and ADC(2)/TZVP levels proves that the semiempirical OM2/MRCI method gives a reasonable description of the excited states for the PΦB model.

At the OM2/MRCI level, another S_0/S_1 CI minimum was located ($CI_{01\beta-min}$, 1.66 eV above Pr), which is responsible for the nonadiabatic decay via channel II. $CI_{01\beta-min}$ is characterized by rotation of the whole C–D double-ring moiety around the C10–C11 bond by about 80° from the Pr conformation (Figure 3 and Tables 2 and 3). During this rotation, the angle between rings C and D also decreases by around 10° (τ_{14-15} from -17.5° to -6.0°). In this situation, the C10–C11 bond length increases to 1.45 Å, while the C9–C10 bond becomes shorter to 1.38 Å. Compared with Pr, C10–C11 and C9–C10 tend to become single and double bonds, respectively, at $CI_{01\alpha-min}$. The intramolecular charge transfers also occur at this geometry. The molecular orbitals (Figure S-3 in the Supporting Information) and net atomic charge distributions (Table S-5 in the Supporting Information) support such a conclusion.

One S_1 minimum, $(S_1)_\beta$, also exists in the vicinity of $CI_{01\beta-min}$. The major geometry distinction of $(S_1)_\beta$ and $CI_{01\beta-min}$ is the different C15–C16 twisting angles (τ_{15-16}). From Pr to $(S_1)_\beta$, τ_{15-16} changes from 173.9° to 170.4° , which is much less than

the change from Pr to $\text{CI}_{01\beta\text{-min}}$ (173.9° to -167.1°). Similar to $(\text{S}_1)_\alpha$, the $\text{S}_0\text{--}\text{S}_1$ energy gap of the two states is also very small (only ~ 0.24 eV) at the $(\text{S}_1)_\beta$ geometry, which is also close to the S_0/S_1 CI as discussed above (Table 3).

For illustration, we also constructed the 2D PE surfaces by performing rigid scans along the internal coordinates τ_{10-11} and τ_{14-15} starting from the Pr form (Figure 5). Because the basic features of the two-dimensional S_0 and S_1 surfaces for channel II are very similar to those of channel I, a similar reaction mechanism should be expected. From the Pr conformation, the system can quickly move to the $\text{CI}_{01\beta}$ seam, instead of only $\text{CI}_{01\beta\text{-min}}$ (Figure 5c,d). After the internal conversion to the S_0 state, the system may move forward to $(\text{S}_0)_\beta$ or backward to the Pr conformer. Similar to channel I, both the C10–C11 (τ_{10-11}) and C14–C15 (τ_{14-15}) bonds may perform the twisting motion in the excited-state dynamics.

Generally speaking, both channels may be easily accessible because of the lack of an obvious barrier, while the final destinations of the nonadiabatic dynamics may be quite different. When the molecule decays to the S_0 state via the CI seams, the molecule may rotate forward to the other S_0 minimum [$(\text{S}_0)_\alpha$ or $(\text{S}_0)_\beta$] or just rotate backward to the original Pr conformation. In order to get further insight into the real-time molecular motions for the two channels, the ultrafast nonadiabatic dynamics study is necessary.

3.3. Nonadiabatic Dynamics Study of PΦB. A set of trajectories was used in the surface-hopping nonadiabatic dynamics study at the OM2/MRCI level. Starting from the Pr configuration, the fractional occupation of the S_1 state shows an ultrafast decay (Figure 6). More than 50% of the trajectories jump to the S_0 state within 300 fs, and most of the trajectories decay to the S_0 state within 500 fs.

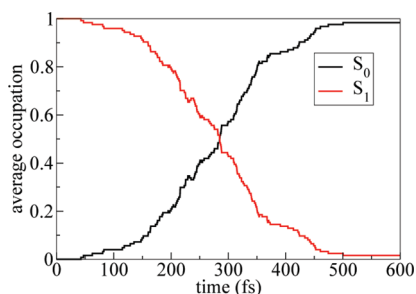


Figure 6. Time-dependent average fractional occupations of electronic states for nonadiabatic dynamics initiated from the Pr conformation.

To inspect the details of the nonadiabatic transitions, the geometrical distributions of two key internal coordinates (τ_{9-10} and τ_{10-11}) were constructed for all of the initial geometries and hopping geometries, as shown in Figure 7. Because all of the initial geometries are sampled in the vicinity of the Pr configuration, the absolute values of the angles around both central C–C bonds (C9–C10 and C10–C11) between rings B and C are distributed around 170° at $t = 0$ (Figure 7a). Then trajectories move on the S_1 state and access the CI seams ($\text{CI}_{01\alpha}$ or $\text{CI}_{01\beta}$), where the $\text{S}_1 \rightarrow \text{S}_0$ hop takes place. Clearly, two reaction channels can be identified immediately in Figure 7b. Many trajectories (74.1%) pass $\text{CI}_{01\alpha}$ by a twisting motion of the C9–C10 bond, while some trajectories (22.8%) access $\text{CI}_{01\beta}$ with the twisting motion of the C10–C11 bond. We did not observe other motions such as the Hula twist of the C9–C10 and C10–C11 bonds.

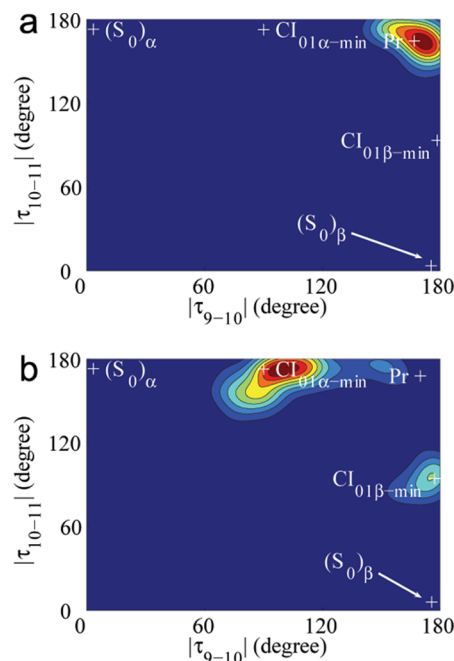


Figure 7. Geometrical distributions as functions of the C9–C10 (τ_{9-10}) and C10–C11 (τ_{10-11}) angles over (a) all initial geometries and (b) hopping geometries.

As shown in the reaction pathways, the trajectories via the two CIs result in quite different products (Figure 8). Many

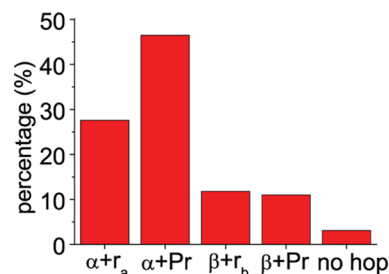


Figure 8. Ratio distributions of trajectories toward different reaction channels. “ $\alpha+\text{r}_a$ ” denotes the trajectories passing $\text{CI}_{01\alpha}$ and moving to $(\text{S}_0)_\alpha$; “ $\alpha+\text{Pr}$ ” refers to the trajectories passing $\text{CI}_{01\alpha}$ and rotating back to Pr conformation; “ $\beta+\text{r}_b$ ” denotes the trajectories passing $\text{CI}_{01\beta}$ and moving to $(\text{S}_0)_\beta$; “ $\beta+\text{Pr}$ ” refers to trajectories passing $\text{CI}_{01\beta}$ and rotating back to Pr conformation; “no hop” refers to the trajectories that did not hop.

trajectories (74.1%) jump back to the ground state via $\text{CI}_{01\alpha}$. After the $\text{S}_1 \rightarrow \text{S}_0$ hop, two-thirds of these trajectories return back to the Pr conformation (46.5%) and only one-third (27.6%) move toward to $(\text{S}_0)_\alpha$. There are also many trajectories (22.8%) passing $\text{CI}_{01\beta}$. Among them, the numbers of trajectories that move backward to Pr (11.0%) and forward to $(\text{S}_0)_\beta$ (11.8%) are similar. Only a very small number of trajectories do not decay to the S_0 state (3.1%), and thus, this channel is negligible. For the current system, we did not observe any trajectory passing other reaction channels characterized by the significant C4–C5 or C15–C16 twist. This finding is consistent with the mechanism suggested by previous reaction-path calculations at various levels of electronic-structure theory.^{2,28,30}

Since the CI seams (not only the CI minima) are accessible in the excited state, it is necessary to determine the relevant

internal coordinates involved in the nonadiabatic dynamics. For this purpose, we investigated the details of the nuclear distributions at different time.

For channel I, we plotted the time-dependent geometrical distributions as functions of the internal coordinates τ_{9-10} and τ_{5-6} , which describe the rotations around C9–C10 and C5–C6 respectively (Figure 9). Within the first 100 fs, the trajectories

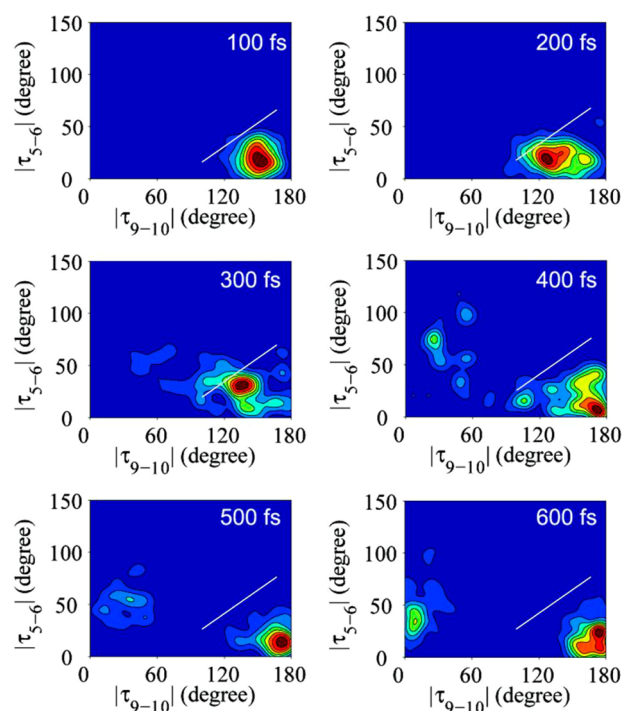


Figure 9. Geometrical distributions as functions of the twisting angles around C9–C10 (τ_{9-10}) and C5–C6 (τ_{5-6}) at different time steps for all of the trajectories passing $CI_{01\alpha}$. The white lines in the plots refer to the positions of the $CI_{01\alpha}$ seam.

remain the Pr conformation. At 300 fs, many trajectories reach the $CI_{01\alpha}$ seam region. During this process, the twisting motions of the C9–C10 and C5–C6 bonds are observed. Such detailed molecular motion can be examined again carefully from Figure 10. At the Pr configuration, the twisting angles of C9–C10 (τ_{9-10} , between rings B and C) and C5–C6 (τ_{5-6} , between rings A and B) are -167.9° and -17.9° , respectively. At a typical hopping geometry, these angles become -114.8° and -13.8° , respectively. Thus, rings A and B cannot be treated as a single moiety performing an overall rotation during the excited-state motion; otherwise, twisting motion of C5–C6 should not be observed. Instead, the rotations of rings A and B take place in a nonsynchronous way. At $CI_{01\alpha-min}$, the above two angles become -91.5° and -7.8° , respectively. The two relevant angles (the C9–C10 twisting angle and the ring A/ring B angle) show quite a difference at the above typical hopping geometry and $CI_{01\alpha-min}$. Thus, not the CI minimum geometry ($CI_{01\alpha-min}$) but the $CI_{01\alpha}$ seam (Figures 4 and 10) is responsible for the nonadiabatic decay of the PΦB model. After the $S_1 \rightarrow S_0$ hop, the forward and backward internal rotations around the C9–C10 bond finally result in the photoproduct (S_0)_α and the original Pr conformation, respectively.

For channel II, we plotted the time-dependent geometrical distributions of the relevant internal coordinates τ_{10-11} and τ_{14-15} , which refer to the rotations around the C10–C11 and

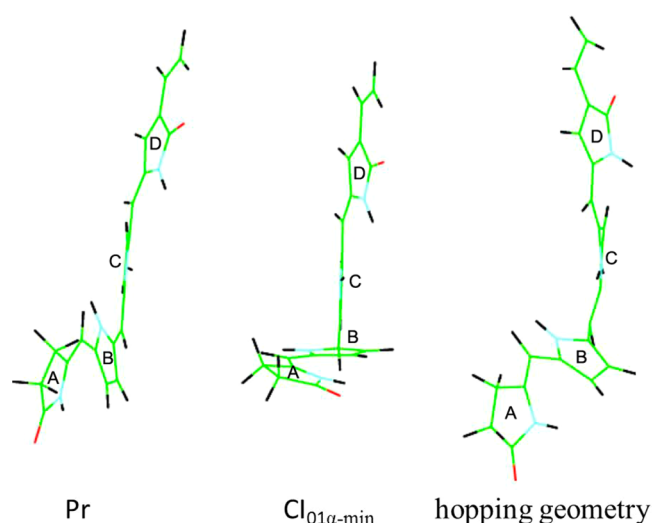


Figure 10. Structures of Pr, $CI_{01\alpha-min}$, and a typical hopping geometry.

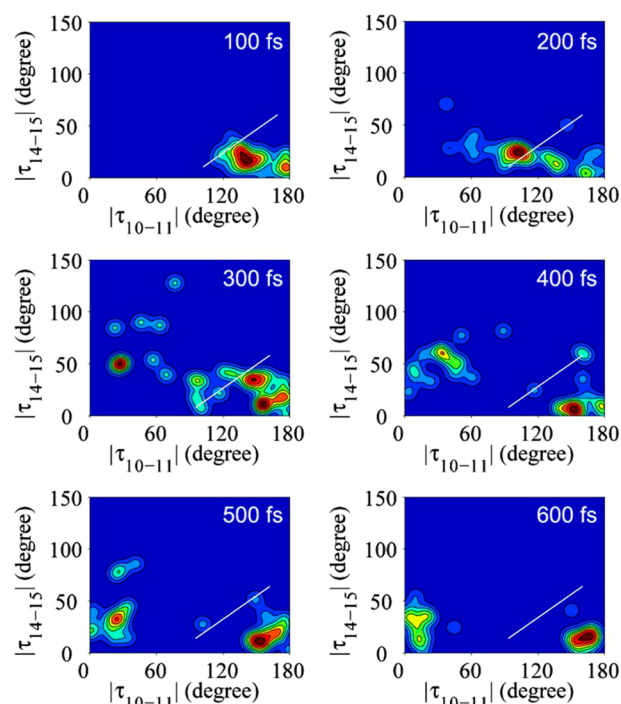


Figure 11. Geometrical distributions as functions of the twisting angles around C10–C11 (τ_{10-11}) and C14–C15 (τ_{14-15}) at different time steps for all of the trajectories passing $CI_{01\beta}$. The white lines in the plots refer to the positions of the $CI_{01\beta}$ seam.

C14–C15 bonds, respectively, as shown in Figure 11. Similar to channel I, in the early stage of the dynamics, all of the trajectories remain the Pr conformation. As time progresses, the internal rotations around C10–C11 (τ_{10-11}) and C14–C15 (τ_{14-15}) are involved in the motion (Figure 12). Similarly, the CI seam (instead of only $CI_{01\beta-min}$) is reached. After the $S_1 \rightarrow S_0$ hop, the trajectories also show two different types of motions. The backward internal rotation around C10–C11 gives the Pr conformation, while the successive forward internal rotation around C10–C11 results in the (S_0)_β product.

In our nonadiabatic dynamics study, the model compound of the PΦB in the gas phase displays a different reaction mechanism from the actual chromophore in protein environ-

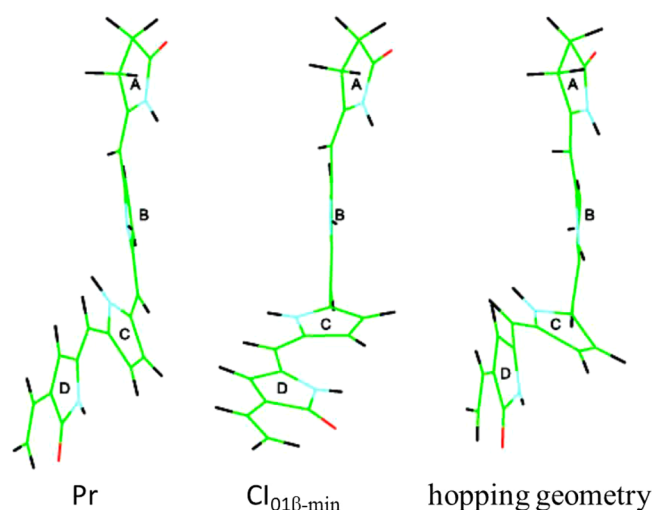


Figure 12. Structures of Pr, $CI_{01\beta\text{-min}}$, and a typical hopping geometry.

ments. Consistent with the references' reports,^{2,28,30} we did not observe the pathways along the rotation around the C4–C5 or C15–C16 bonds. Instead, only two reaction channels were found: the rotations around C9–C10 and C5–C6 or the rotations around C10–C11 and C14–C15. Both of these reaction channels seem to be easily accessed because of the lack of an obvious barrier. For the PΦB model, the C–D double-ring moiety is much heavier than the A–B double-ring moiety because of the ethenyl group in ring D, so the former has the larger moment of inertia. This may explain why channel I is preferred over channel II.

Obviously, the one-dimensional picture used to understand the reaction mechanism (including the CI minimum, the one-dimensional reaction pathway, and leading reaction coordinates) is still qualitatively reasonable. This idea can be furthermore supported by the reaction pathway (Figure S-2 in the Supporting Information) and hopping geometry distribution (Figure S-4 in the Supporting Information). However, a more precise mechanism would involve more details, such as the involvement of other nuclear motions and the topology of the CI seams. As discussed in the literature, this feature seems to widely exist in different molecular systems.⁵⁴ The deep understanding of this issue certainly requires an exploration of the topologies of complex multidimensional PE surfaces and subsequent nonadiabatic dynamics.⁵⁴

4. CONCLUSIONS

The primary event of the photoinduced isomerization reaction of the PΦB model in vacuo was simulated using surface-hopping nonadiabatic dynamics at the semiempirical OM2/MRCI level. Two reaction channels (via $CI_{01\alpha}$ and $CI_{01\beta}$) were found to be responsible for the excited-state decay, which are mainly characterized by the rotations around the C9–C10 and C10–C11 bonds, respectively.

In the surface-hopping simulations, the decay of the S_1 population is an ultrafast process (within 500 fs) because of the lack of barriers on the reaction pathways. The reaction mechanism is described as shown in Figure 13. Most trajectories pass $CI_{01\alpha}$ (74.1%), which is characterized by the twisting motion of the C9–C10 bond, while less than 25% of the trajectories pass $CI_{01\beta}$, which displays the twisting motion of the C10–C11 bond. For the $CI_{01\alpha}$ channel, after the trajectories decay to the S_0 state, only one-third of them move forward to $(S_0)_\alpha$ while two-thirds of them move backward to Pr. For the $CI_{01\beta}$ channel, after the trajectories decay to the S_0 state, the numbers of trajectories following the forward channel [to $(S_0)_\beta$] and the backward channel (to Pr) seem rather similar. No matter which pathway is followed, the nonadiabatic decay always involves a part of the CI seam instead of only the CI minimum. Therefore, the molecular motions on the excited state also involve other twisting motions, for instance the rotations of rings A and D. In this sense, we can conclude that the simple minimum-energy reaction pathway calculation is not enough to correctly locate the internal coordinates responsible for the nonadiabatic decay for PΦB in the gas phase.

Although our work can provide a very clear picture of the photoisomerization process of PΦB in vacuo, we know that the reaction dynamics is different from that in protein environments. This means that the reaction mechanism may be modified by the special constraints of protein environments, including steric hindrance, hydrogen-bonding networks, anisotropic electrostatic interactions, and charge status. In such protein environments, the steric interactions may block the fast internal conversion processes that exist in the gas phase. Thus, to simulate the photoinduced Pr → Pfr conversion of PΦB in plants, the protein environments must be considered. In this case, the hybrid QM/MM approach may be a suitable choice to deal with such complex reactions. This certainly represents a very challenging task and will be the subject of future research.

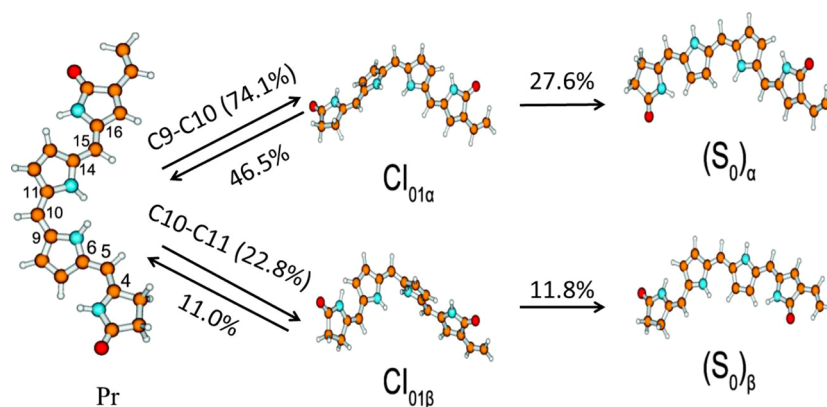


Figure 13. Final mechanistic scheme and quantum yields of photochemical reactions of PΦB from the Pr conformation in the gas phase.

■ ASSOCIATED CONTENT

■ Supporting Information

Figures showing the Pr geometry, one-dimensional potential surfaces, molecular orbitals, and the distribution of hopping geometries and tables of representative internal coordinates, optimization results at the PLA at TDDFT levels, geometry distributions for different reaction channels, net atomic charges, and Cartesian coordinates of all important geometries. This material is available free of charge via the Internet at <http://pubs.acs.org>.

■ AUTHOR INFORMATION

Corresponding Author

*Fax: +86-532-80662778. Tel: +86-532-80662630. E-mail: lanzg@qibebt.ac.cn.

Notes

The authors declare no competing financial interest.

■ ACKNOWLEDGMENTS

This work was supported by the CAS 100 Talents Project, the National Natural Science Foundation of China (Grant Nos. 21103213 and 91233106), and the Director Innovation Foundation of CAS-QIBEBT. The authors thank the Supercomputing Center, Computer Network Information Center, CAS, and the supercomputational center of CAS-QIBEBT for providing computational resources.

■ REFERENCES

- (1) Rockwell, N. C.; Su, Y.-S.; Lagarias, J. C. Phytochrome Structure and Signaling Mechanisms. *Annu. Rev. Plant Biol.* **2006**, *57*, 837–858.
- (2) Altoè, P.; Climent, T.; De Fusco, G. C.; Stenta, M.; Bottoni, A.; Serrano-Andriés, L.; Merchán, M.; Orlandi, G.; Garavelli, M. Deciphering Intrinsic Deactivation/Isomerization Routes in a Phytochrome Chromophore Model. *J. Phys. Chem. B* **2009**, *113*, 15067–15073.
- (3) Alvey, R. M.; Biswas, A.; Schluchter, W. M.; Bryant, D. A. Attachment of Noncognate Chromophores to CpcA of *Synechocystis* sp. PCC 6803 and *Synechococcus* sp. PCC 7002 by Heterologous Expression in *Escherichia coli*. *Biochemistry* **2011**, *50*, 4890–4902.
- (4) Bongards, C.; Gärtner, W. The Role of the Chromophore in the Biological Photoreceptor Phytochrome: An Approach Using Chemically Synthesized Tetrapyrroles. *Acc. Chem. Res.* **2010**, *43*, 485–495.
- (5) Wagner, J. R.; Brunzelle, J. S.; Forest, K. T.; Vierstra, R. D. A Light-Sensing Knot Revealed by the Structure of the Chromophore-Binding Domain of Phytochrome. *Nature* **2005**, *438*, 325–331.
- (6) Wagner, J. R.; Zhang, J.; Brunzelle, J. S.; Vierstra, R. D.; Forest, K. T. High Resolution Structure of *Deinococcus* Bacteriophytochrome Yields New Insights into Phytochrome Architecture and Evolution. *J. Biol. Chem.* **2007**, *282*, 12298–12309.
- (7) Yang, X.; Stojković, E. A.; Kuk, J.; Moffat, K. Crystal Structure of the Chromophore Binding Domain of an Unusual Bacteriophytochrome, RpbPhP3, Reveals Residues That Modulate Photoconversion. *Proc. Natl. Acad. Sci. U.S.A.* **2007**, *104*, 12571–12576.
- (8) Essen, L.-O.; Mailliet, J.; Hughes, J. The Structure of a Complete Phytochrome Sensory Module in the Pr Ground State. *Proc. Natl. Acad. Sci. U.S.A.* **2008**, *105*, 14709–14714.
- (9) Cornilescu, G.; Uliasz, A. T.; Cornilescu, C. C.; Markley, J. L.; Vierstra, R. D. Solution Structure of a Cyanobacterial Phytochrome GAF Domain in the Red-Light-Absorbing Ground State. *J. Mol. Biol.* **2008**, *383*, 403–413.
- (10) Van Thor, J. J.; Mackeen, M.; Kuprov, I.; Dwek, R. A.; Wormald, M. R. Chromophore Structure in the Photocycle of the Cyanobacterial Phytochrome Cph1. *Biophys. J.* **2006**, *91*, 1811–1822.
- (11) Mroginski, M. A.; Murgida, D. H.; von Stetten, D.; Kneip, C.; Mark, F.; Hildebrandt, P. Determination of the Chromophore Structures in the Photoinduced Reaction Cycle of Phytochrome. *J. Am. Chem. Soc.* **2004**, *126*, 16734–16735.
- (12) Mroginski, M. A.; Murgida, D. H.; Hildebrandt, P. The Chromophore Structural Changes During the Photocycle of Phytochrome: A Combined Resonance Raman and Quantum Chemical Approach. *Acc. Chem. Res.* **2007**, *40*, 258–266.
- (13) Uliasz, A. T.; Cornilescu, G.; Cornilescu, C. C.; Zhang, J.; Rivera, M.; Markley, J. L.; Vierstra, R. D. Structural Basis for the Photoconversion of a Phytochrome to the Activated Pfr Form. *Nature* **2010**, *463*, 250–254.
- (14) Andel, F.; Lagarias, J. C.; Mathies, R. A. Resonance Raman Analysis of Chromophore Structure in the Lumi-R Photoproduct of Phytochrome. *Biochemistry* **1996**, *35*, 15997–16008.
- (15) Durbeej, B.; Borg, O. A.; Eriksson, L. A. Phytochromobilin C15-Z_{syn} → C15-E_{anti} Isomerization: Concerted or Stepwise? *Phys. Chem. Chem. Phys.* **2004**, *6*, 5066–5073.
- (16) Fischer, A. J.; Lagarias, J. C. Harnessing Phytochrome's Glowing Potential. *Proc. Natl. Acad. Sci. U.S.A.* **2004**, *101*, 17334–17339.
- (17) Freer, L. H.; Kim, P. W.; Corley, S. C.; Rockwell, N. C.; Zhao, L.; Thibert, A. J.; Lagarias, J. C.; Larsen, D. S. Chemical Inhomogeneity in the Ultrafast Dynamics of the DXCF Cyanobacteriochrome Tr0924. *J. Phys. Chem. B* **2012**, *116*, 10571–10581.
- (18) Hahn, J.; Strauss, H. M.; Schmieder, P. Heteronuclear NMR Investigation on the Structure and Dynamics of the Chromophore Binding Pocket of the Cyanobacterial Phytochrome Cph1. *J. Am. Chem. Soc.* **2008**, *130*, 11170–11178.
- (19) Hasegawa, J.-y.; Isshiki, M.; Fujimoto, K.; Nakatsuji, H. Structure of Phytochromobilin in the Pr and Pfr Forms: SAC-CI Theoretical Study. *Chem. Phys. Lett.* **2005**, *410*, 90–93.
- (20) Murgida, D. H.; von Stetten, D.; Hildebrandt, P.; Schwinté, P.; Siebert, F.; Sharda, S.; Gärtner, W.; Mroginski, M. A. The Chromophore Structures of the Pr States in Plant and Bacterial Phytochromes. *Biophys. J.* **2007**, *93*, 2410–2417.
- (21) Matute, R. A.; Contreras, R.; Pérez-Hernández, G.; González, L. The Chromophore Structure of the Cyanobacterial Phytochrome Cph1 As Predicted by Time-Dependent Density Functional Theory. *J. Phys. Chem. B* **2008**, *112*, 16253–16256.
- (22) Kaminski, S.; Mroginski, M. A. Molecular Dynamics of Phycocyanobilin Binding Bacteriophytochromes: A Detailed Study of Structural and Dynamic Properties. *J. Phys. Chem. B* **2010**, *114*, 16677–16686.
- (23) Matute, R. A.; Contreras, R.; González, L. Time-Dependent DFT on Phytochrome Chromophores: A Way to the Right Conformer. *J. Phys. Chem. Lett.* **2010**, *1*, 796–801.
- (24) Mroginski, M. A.; Kaminski, S.; von Stetten, D.; Ringsdorf, S.; Gärtner, W.; Essen, L.-O.; Hildebrandt, P. Structure of the Chromophore Binding Pocket in the Pr State of Plant Phytochrome phyA. *J. Phys. Chem. B* **2011**, *115*, 1220–1231.
- (25) Borg, O. A.; Durbeej, B. Which Factors Determine the Acidity of the Phytochromobilin Chromophore of Plant Phytochrome? *Phys. Chem. Chem. Phys.* **2008**, *10*, 2528–2537.
- (26) Borg, O. A.; Durbeej, B. Relative Ground and Excited-State pK_a Values of Phytochromobilin in the Photoactivation of Phytochrome: A Computational Study. *J. Phys. Chem. B* **2007**, *111*, 11554–11565.
- (27) Durbeej, B.; Eriksson, L. A. Protein-Bound Chromophores Astaxanthin and Phytochromobilin: Excited State Quantum Chemical Studies. *Phys. Chem. Chem. Phys.* **2006**, *8*, 4053–4071.
- (28) Durbeej, B. On the Primary Event of Phytochrome: Quantum Chemical Comparison of Photoreactions at C4, C10 and C15. *Phys. Chem. Chem. Phys.* **2009**, *11*, 1354–1361.
- (29) Durbeej, B.; Borg, O. A.; Eriksson, L. A. Computational Evidence in Favor of a Protonated Chromophore in the Photoactivation of Phytochrome. *Chem. Phys. Lett.* **2005**, *416*, 83–88.
- (30) Strambi, A.; Durbeej, B. Initial Excited-State Relaxation of the Bilin Chromophores of Phytochromes: A Computational Study. *Photochem. Photobiol. Sci.* **2011**, *10*, 569–579.
- (31) Tully, J. C. Molecular Dynamics with Electronic Transitions. *J. Chem. Phys.* **1990**, *93*, 1061–1071.

- (32) Hammes-Schiffer, S.; Tully, J. C. Proton Transfer in Solution: Molecular Dynamics with Quantum Transitions. *J. Chem. Phys.* **1994**, *101*, 4657–4667.
- (33) Fabiano, E.; Keal, T. W.; Thiel, W. Implementation of Surface Hopping Molecular Dynamics using Semiempirical Methods. *Chem. Phys.* **2008**, *349*, 334–347.
- (34) Weber, W.; Thiel, W. Orthogonalization Corrections for Semiempirical Methods. *Theor. Chem. Acc.* **2000**, *103*, 495–506.
- (35) Weber, W. Ein Neues Semiempirisches NDDO-Verfahren mit Orthogonalisierungskorrekturen: Entwicklung des Modells, Implementierung, Parametrisierung und Anwendungen, 1996.
- (36) Otte, N.; Scholten, M.; Thiel, W. Looking at Self-Consistent-Charge Density Functional Tight Binding from a Semiempirical Perspective. *J. Phys. Chem. A* **2007**, *111*, 5751–5755.
- (37) Koslowski, A.; Beck, M. E.; Thiel, W. Implementation of a General Multireference Configuration Interaction Procedure with Analytic Gradients in a Semiempirical Context Using the Graphical Unitary Group Approach. *J. Comput. Chem.* **2003**, *24*, 714–726.
- (38) Barbatti, M.; Lan, Z.; Crespo-Otero, R.; Szymczak, J. J.; Lischka, H.; Thiel, W. Critical Appraisal of Excited State Nonadiabatic Dynamics Simulations of 9H-adenine. *J. Chem. Phys.* **2012**, *137*, No. 22A503.
- (39) Kazaryan, A.; Lan, Z.; Schäfer, L. V.; Thiel, W.; Filatov, M. Surface Hopping Excited-State Dynamics Study of the Photoisomerization of a Light-Driven Fluorene Molecular Rotary Motor. *J. Chem. Theory Comput.* **2011**, *7*, 2189–2199.
- (40) Zhuang, X.; Wang, J.; Lan, Z. Photoinduced Nonadiabatic Decay and Dissociation Dynamics of Dimethylnitramine. *J. Phys. Chem. A* **2013**, *117*, 4785–4793.
- (41) Lan, Z.; Fabiano, E.; Thiel, W. Photoinduced Nonadiabatic Dynamics of Pyrimidine Nucleobases: On-the-Fly Surface-Hopping Study with Semiempirical Methods. *J. Phys. Chem. B* **2009**, *113*, 3548–3555.
- (42) Lan, Z.; Lu, Y.; Weingart, O.; Thiel, W. Nonadiabatic Decay Dynamics of a Benzylidene Malononitrile. *J. Phys. Chem. A* **2012**, *116*, 1510–1518.
- (43) Zhang, W.; Lan, Z.; Sun, Z.; Gaffney, K. J. Resolving Photo-Induced Twisted Intramolecular Charge Transfer with Vibrational Anisotropy and TDDFT. *J. Phys. Chem. B* **2012**, *116*, 11527–11536.
- (44) Thiel, W. MNDO Program, version 6.1, 2007.
- (45) Frisch, M. J.; Trucks, G. W.; Schlegel, H. B.; Scuseria, G. E.; Robb, M. A.; Cheeseman, J. R.; Scalmani, G.; Barone, V.; Mennucci, B.; Petersson, G. A.; Nakatsuji, H.; Caricato, M.; et al. *Gaussian 09*; Gaussian, Inc.: Wallingford, CT, 2009.
- (46) Ahlrichs, R.; Bär, M.; Häser, M.; Horn, H.; Kölmel, C. Electronic Structure Calculations on Workstation Computers: The Program System Turbomole. *Chem. Phys. Lett.* **1989**, *162*, 165–169.
- (47) Bearpark, M. J.; Robb, M. A.; Schlegel, H. B. A Direct Method for the Location of the Lowest Energy Point on a Potential Surface Crossing. *Chem. Phys. Lett.* **1994**, *223*, 269–274.
- (48) Yarkony, D. R. Diabolical Conical Intersections. *Rev. Mod. Phys.* **1996**, *68*, 985–1013.
- (49) Keal, T.; Koslowski, A.; Thiel, W. Comparison of Algorithms for Conical Intersection Optimisation Using Semiempirical Methods. *Theor. Chem. Acc.* **2007**, *118*, 837–844.
- (50) Schirmer, J. Beyond the Random-Phase Approximation: A New Approximation Scheme for the Polarization Propagator. *Phys. Rev. A* **1982**, *26*, 2395–2416.
- (51) Schafer, A.; Huber, C.; Ahlrichs, R. Fully Optimized Contracted Gaussian Basis Sets of Triple Zeta Valence Quality for Atoms Li to Kr. *J. Chem. Phys.* **1994**, *100*, 5829–5835.
- (52) Lee, C.; Yang, W.; Parr, R. G. Development of the Colle–Salvetti Correlation-Energy Formula into a Functional of the Electron Density. *Phys. Rev. B* **1988**, *37*, 785–789.
- (53) Becke, A. D. Density-Functional Thermochemistry. III. The Role of Exact Exchange. *J. Chem. Phys.* **1993**, *98*, 5648–5652.
- (54) Robb, M. A. Conical Intersections in Organic Photochemistry. In *Conical Intersections II: Theory, Computation and Experiment*; Domcke, W., Yarkony, D. R., Köppel, H., Eds.; World Scientific: Singapore, 2011; Chapter 1.